Revision 2

Inclusions in calcite phantom crystals suggest role of clay minerals in dolomite formation

Stefan Farsang[1*], Péter Pekker[2], Giulio I. Lampronti[1], Zsombor Molnár[2], Rastislav Milovský[3], Mihály Pósfai[2], Daniel Ozdín[4], Timothy D. Raub[5], and Simon A. T. Redfern[6]

[1]Department of Earth Sciences, University of Cambridge, Downing Street, Cambridge, CB2 3EQ, UK (*sf571@cam.ac.uk)

[2]Research Institute of Biomolecular and Chemical Engineering, University of Pannonia, 8200 Veszprém, Egyetem u. 10., Hungary

[3]Earth Science Institute, Slovak Academy of Sciences, Ďumbierska 1, 974 11 Banská Bystrica, Slovakia

[4]Department of Mineralogy, Petrology and Economic Geology, Faculty of Natural Sciences, Comenius University, Ilkovičova 6, 842 15 Bratislava, Slovakia

[5]School of Earth & Environmental Sciences, University of St Andrews, Irvine Building, St Andrews, KY16 9AL, UK

[6]Asian School of the Environment, Nanyang Technological University, 50 Nanyang Avenue, 639798, Singapore

Abstract

Micro- and nano-inclusions embedded in calcite phantom crystals from Gemerská Ves, Slovakia, have been characterized by a combination of Raman spectroscopy, scanning and transmission

electron microscopy, X-ray powder diffraction, and C and O isotope analysis. Whereas the outer, colorless part of the phantom crystal is relatively homogeneous, cavity and inclusion-free, the inner, terracotta-colored part contains abundant cavities, dolomite, hematite, goethite, titanite, phyllosilicates (mainly kaolinite and illite), and apatite inclusions and nanostructures that have formed on the walls of cavities. The nanostructures comprise hematite and goethite particles sandwiched between either two phyllosilicate crystals or a phyllosilicate and a carbonate (calcite or dolomite) crystal. Our observations suggest that all inclusions in the terracotta calcite originate from the terra rossa (a common soil type in karstic areas) and limestone outcropping adjacent to the calcite crystals. While the μm-sized phyllosilicate and hematite particles were likely transported from the terra rossa and attached to the surface of growing calcite, the presence of phyllosilicates that are only a few atomic layers thick and of euhedral hematite, goethite and dolomite crystals suggests that these particles precipitated along with the phantom calcite in situ, from an aqueous solution carrying terra rossa-derived and limestone-derived solutes. The compositional differences between the terra rossa (e.g., smectite as the only major Mg-rich phase) and terracotta calcite inclusions (e.g., dolomite as the only major Mg-rich phase and the presence of only Mg-free clays) hint that a smectite-illite conversion provides the Mg necessary for the precipitation of dolomite and possibly the Fe associated with the iron oxyhydroxide nanostructures. Phyllosilicate nucleation on calcite and dolomite nucleation on phyllosilicates, as inferred from nanoscale mineralogical associations, suggest that carbonates and phyllosilicates may mutually enhance nucleation and growth. This enhancement may result in the formation of large-scale clay-carbonate successions in aqueous settings, including the enigmatic, pink-colored cap dolostones succeeding late Neoproterozoic “Snowball Earth” deposits. The distribution of inclusions in the terracotta calcite and the preferred nucleation of hematite and goethite on

phyllosilicate, rather than on carbonate surfaces, indicates that phyllosilicates have a potential to not only disrupt crystal growth and trigger the formation of cavities in the structure of the calcite host, but also to provide surfaces for the precipitation of different phases in the cavities and to uniformly distribute otherwise incompatible materials in a calcite host crystal. This calls for further exploration of the potential application of phyllosilicates in composite structure development.

Keywords

Calcite, cap carbonate, clay, dolomite, hematite, goethite, illite, kaolinite, nanoparticle, nucleation, phantom crystal, phyllosilicate, Raman spectroscopy, SEM, Snowball Earth, TEM, XRD

Introduction

A phantom crystal is a crystal embedded in another crystal of the same mineral species with visible outlines. The embedded crystal is visible due to some variation in composition (e.g., substitution of atoms, presence of inclusions) or the attachment of particles to its surface. Examples include quartz (SiO_2) phantom crystals outlined by green chlorite from Comechas em Cima, Serra do Cabral, Minas Gerais, Brazil, by green fuchsite from Ihovitra, Ambatofinandrahna, Madagascar, by white clay minerals from Santo Antonio mine, Serra do Cabral, Minas Gerais, Brazil, by black manganese minerals from Alegre mine, near Mimoso, Bahia, Brazil and calcite ($CaCO_3$) phantom crystals outlined by pyrite from Korsnas mine,

Finland and the Surneshko Kladenche copper vein deposit, Rossen Ore Field, Bulgaria and by dark red hematite from Chihuahua state, Mexico (Johnston and Butler 1946; Sinkankas 1966; Rehtijärvi and Kinnunen 1979; Gornitz 1981; Bonev et al. 2005; Farfan and Post 2019). In the latter, the pre-existing calcite crystals are scalenohedra coated with dark red hematite (Fe_2O_3), which are overgrown by transparent rhombohedra (Sinkankas 1966; Gornitz 1981). Calcite phantom crystals originating from Gemerská Ves, Slovakia, have a distinct terracotta color (Fig. 1) and display a range of crystal forms, the most abundant being scalenohedra, hexagonal prisms, and rhombohedra, while these forms are usually shared by the embedded and embedding crystals (Bálintová et al. 2006). Here, we characterize inclusions of these calcite phantom crystals by size, distribution and mineralogy and propose a formation scenario for the phantom crystals.

Methods

Raman spectroscopy

A confocal LabRAM 300 (Horiba Jobin Yvon) Raman spectrometer with 300 mm focal length objective, at the Department of Earth Sciences, University of Cambridge, was used to collect Raman spectra from 100 to 1800 cm^{-1}. A holographic grating of 1800 $gr.mm^{-1}$ coupled to a Peltier front illuminated CCD detector (1024 × 256 pixel in size) enabled a spectral resolution of ~1 cm^{-1}. The excitation line at 532.05 nm was produced by a Ventus 532 laser source (Laser Quantum) focused on the sample using an Olympus LMPLFLN 50× long working distance objective.

All Raman spectra were treated using PeakFit software. For each Raman spectrum, the baseline was subtracted, and peak features were determined by least squares fitting to Voigt profiles for each Raman band. Peak positions were calibrated against the measured excitation of a Ne light emission reference spectrum (Saloman and Sansonetti 2004).

Scanning electron microscopy (SEM)

For SEM analysis, a phantom calcite sample mounted in epoxy was polished with colloidal silica, carbon-coated and analyzed under high-vacuum conditions. A FEI Quanta 650F instrument equipped with two Bruker XFlash 6|30 silicon drift EDX detectors at the Department of Earth Sciences, University of Cambridge was employed for back-scattered electron (BSE) imaging and for qualitative chemical analysis by energy-dispersive spectroscopy (EDS). An accelerating voltage of 15 keV, beam spot size of 4.5, and working distance of 13 mm was used.

To investigate the mineralogical makeup of terra rossa, it was powdered and deposited on amorphous carbon support film. An FEI Apreo LoVac instrument equipped with an EDAX METEK Octane Elect Plus EDX detector at the Department of Material Sciences, University of Pannonia was employed for back-scattered electron (BSE) imaging and for qualitative chemical analysis by energy-dispersive spectroscopy (EDS). An accelerating voltage of 20 keV, beam spot size of 4.5, and working distance of 10 mm was used.

Transmission electron microscopy (TEM)

Two samples were prepared for TEM analysis. The first was prepared by depositing a drop of aqueous suspension of the ground particles of the terracotta-colored calcite onto a 200 mesh copper TEM grid covered by a lacey carbon amorphous support film. The second sample was a section of terracotta colored calcite cut perpendicular to the growth lines and mounted in a 3 mm Cu support ring. The sample was thinned to 50 μm and then ion milled.

TEM analyses were performed using a Talos F200X G2 instrument (Thermo Fisher Scientific) at the Nanolab, University of Pannonia. The instrument is equipped with a field-emission gun, a Ceta 16M camera, and a four-detector Super-X energy-dispersive X-ray spectrometer and is capable of working in both conventional TEM and scanning transmission (STEM) modes. The instrument was operated at 200 kV accelerating voltage. Low-magnification bright-field (BF) images, high-resolution (HRTEM) images and selected-area electron diffraction (SAED) patterns were obtained in TEM mode. STEM high-angle annular dark-field (HAADF) images were collected both for high-resolution structure analyses and for mapping elemental compositions by coupling STEM imaging with energy-dispersive X-ray spectrometry (EDS).

X-ray powder diffraction (XRD)

XRD was conducted at the Department of Earth Sciences, University of Cambridge. Powder diffraction data of breccia were collected from 10 to 60˚2θ (0.02˚ step size) in Bragg-Brentano geometry on a D8 Advance Bruker powder diffractometer using Mo Kα X-rays and a LYNXEYE XE-T position sensitive detector. Powder diffraction data of terra rossa were collected from 4 to 50˚2θ (0.04˚ step size) in Bragg-Brentano geometry on a D8 Advance Bruker powder diffractometer using Cu Kα radiation and a Vantec position sensitive detector.

Rietveld refinements were performed using TOPAS-Academic V6 (Coelho 2018). Starting crystal structures of all mineral phases were retrieved from the Inorganic Crystal Structure Database (Allmann and Hinek 2007). Instrumental parameters were modelled by refining data collected from a LaB_6 660b NIST standard. A shifted Chebyshev function with eight parameters was used to fit the background. The peak shape was modelled using a Pseudo-Voigt function. The March-Dollase model was used to correct for preferred orientation on the following crystallographic planes: (1 0 4) for calcite; (0 0 1) for kaolinite, illite, and montmorillonite; and (1 0 0) for goethite. The refinement converged to a final χ^2 and R_{wp} of 6.73 and 16.04%, respectively for the breccia, and 2.04 and 2.49%, respectively for the terra rossa.

C and O isotopes

C and O stable isotope ratios were measured using a Gasbench III preparation device coupled to isotope-ratio mass-spectrometer MAT 253 (both ThermoFisher Scientific). Microdrilled samples of calcite (60-80 micrograms) were loaded into 5mL borosilicate glass vials (Labco), sealed by caps with rubber septa and flushed with helium to remove atmosphere. Subsequent phosphoric acid digestion (McCrea 1950) took place at 40 °C overnight. The evolved CO_2 gas was analyzed in continuous-flow mode in helium as carrier gas. In each run, three reference gas peaks were followed by four pulses of sample CO_2. Raw isotope ratios were calibrated using an international reference material NBS-18 with $\delta^{13}C$ = +5.014‰, $\delta^{18}O$ = -23.2‰ and two working standards with $\delta^{13}C$ = +2.48‰, $\delta^{18}O$ = -2.40‰ and $\delta^{13}C$ = -9.30‰, $\delta^{18}O$ = -15.30‰, respectively. Typical precision of measurements is 0.1 ‰ for C and 0.2 ‰ for O (1σ). Isotope values are reported as permil with reference to the international standard Vienna Pee Dee Belemnite (VPDB).

Results and discussion

Mineralogy

The phantom calcite was sampled at N 48˚ 29.147' E 20˚ 15.112' in a quarry west of Gemerská Ves village, Revúca county, Banská Bystrica region, Slovakia. The quarry is an outcrop of Middle Triassic Wetterstein limestone (Elečko et al. 1985) with colorless and whitish calcite crystals commonly occurring in its vugs. The massive limestone body is cut by an elongated body of red breccia, up to 5 m wide running NE-SW, that contains cm-sized limestone clasts in a fine-grained, layered matrix composed of terra rossa (a common soil type in karstic areas) and calcium carbonate (Fig. 2). Such rocks are abundant in the region (Slovak karst) and may form by the collapse of cave walls and ceilings (*e.g.*, karst collapse breccia), or can be related to faults in karstic areas (*e.g.*, footwall breccia) (Gaál 2008). Near the limestone-breccia contact, the breccia is consolidated and does not contain euhedral calcite crystals (Fig. 2a,b). In contrast, the central part of the breccia body is rich in vugs that contain calcite crystals up to 10 cm in size (Fig. 2c,d). Calcite crystals growing close (few millimeters) to the terra rossa typically contain a terracotta-colored inner part, while those sitting further away are colorless or whitish without an embedded terracotta crystal (Fig. 2d).

The Raman spectrum of calcite has six peaks corresponding to five Raman-active vibrational modes (translational external E_g, librational external E_g, internal ν_4 E_g, internal ν_1 A_{1g}, and internal ν_3 E_g) and an overtone mode, which represents the $2\nu_2$ overtone mode of the IR-active ν_2 A_{2u} mode (Krishnan 1945; Couture 1947; Krishnamurti 1957; De La Pierre et al. 2014).

The spectrum of our reference material, a natural calcite crystal from Miskolctapolca, Hungary shows features corresponding to these vibrational modes at 158, 284, 713, 1088, 1438, and 1751 cm^{-1}, respectively (Farsang et al. 2018). These six peaks are detected in both the colorless and terracotta-colored part of calcite (Fig. 3a-d). The satellite peaks detected at 1067 and 1066 cm^{-1} in the colorless and terracotta-colored part, respectively, are assigned to isotopic substitutions of ^{13}C and ^{18}O (Cloots 1991).

Hematite possesses seven Raman-active vibrational modes (A_{1g}, E_g, E_g, E_g, E_g, A_{1g}, and E_g) and its Raman spectrum also exhibits the highest-frequency $2E_u$ overtone mode (Beattie and Gilson 1970; Massey et al. 1990; Shim and Duffy 2001). The spectrum of our reference material, a natural hematite crystal from Elba, Tuscany, Italy (Sedgwick Museum of Earth Sciences, University of Cambridge specimen number 822) shows frequency features corresponding to the aforementioned vibrational modes at 224, 243, 290, 294, 404, 497, 604, and 1305 cm^{-1} (Fig. 3e). In the spectrum of terracotta-colored calcite there are clearly visible bands at 225, 408, 503, 608, and 1313 cm^{-1}, while those expected around 243, 290, and 294 cm^{-1} are hidden by the strong signal produced by calcite (Fig. 3d). In the same spectrum there is an additional prominent peak at 659 cm^{-1}. This has only been observed in studies in which the complete symmetry of the hematite structure is lowered either due to partial substitution of Fe atoms, as demonstrated in the case of $Fe_xCr_{2-x}O_3$ ($0 \leq x \leq 2$) solid solution, or by defects induced by stress (McCarty and Boehme 1989; Shim and Duffy 2001). In our case, the very small size of hematite particles (see below) with a significant proportion of atoms located at or near their surface may lead to the lowering of symmetry, giving rise to the peak at 659 cm^{-1}.

Scanning electron microscopy shows that while the colorless part of the crystal is a relatively homogeneous, cavity and inclusion-free calcite, the terracotta-colored part contains

abundant cavities and inclusions of different types, concentrated along growth lines, possibly resulting from episodic calcite growth (Fig. 4a-b). The cavities have irregular shape and range from submicron to several tens of micrometers in size. The largest inclusions are dolomite (Fig. 4c-d), phyllosilicate (Fig. 4e), and apatite (Fig. 4e-f) particles with sizes ranging up to ~50 μm. Smaller inclusions include abundant hematite and rare rutile particles with sizes up to ~5 μm. The dolomite is richer in inclusions than its calcite host and can show an intimate relationship with calcite (Fig. 4c) or occur as euhedral crystals (Fig. 4d). EDS reveals the presence of two types of phyllosilicate: an Al and Si-rich phase (likely kaolinite) and one with additional K (probably illite). The SEM observations are consistent with electron probe microanalysis data of Bálintová et al. (2006) that show slightly elevated levels of MgO, FeO, and MnO in the terracotta-colored part (0.26, 0.04, and 0.02 wt%, respectively, compared to 0.22, 0.01, and 0.01 wt%, in the colorless part).

Sub-micron textural analysis by transmission electron microscopy reveals high abundance and fine-scale distribution of cavities in the terracotta calcite. The walls of these cavities are covered by phyllosilicates, often only a few atomic layers thick, to which submicron and nanosized tabular hematite particles are generally attached (Fig. 5a-c, 6a-b). This explains the presence of bands corresponding to hematite in the Raman spectra from the terracotta part, even when no particles are visible by optical microscopy. Apart from the phyllosilicate-hematite-carbonate sandwich structures, phyllosilicate-hematite-phyllosilicate structures also commonly occur. TEM also reveals the presence of tabular goethite that, just like hematite, is either sandwiched between two phyllosilicate crystals or between a phyllosilicate and a carbonate crystal (Fig. 6c-d). The clearly visible T-O-T sequence of layers, the ~10 Å spacing of these layers (Fig. 5c and 6c), and the high K concentration detected by EDS suggest that at least some

of the phyllosilicate is illite. A very similar association, with nanosized hematite particles sandwiched between illite, has been found in a claystone from Mecsek Mountains, Hungary and seems to be a common nanostructure in Fe and clay-rich environments (Németh et al. 2016). In calcite cavities containing dolomite, the walls of cavities (i.e., the space in between the host calcite and dolomite inclusion) are also covered by phyllosilicate crystals (Fig. 4c-d), suggesting dolomite nucleation and growth may take place on phyllosilicate surfaces. The distinct color of terracotta calcite is likely the result of light scattering produced by the three main mineral phases/groups of inclusions: dark red hematite and whitish dolomite and phyllosilicates.

In order to identify the potential source of particles in the terracotta calcite, the mineralogy of the breccia and terra rossa surrounding the calcite crystals was also analyzed. X-ray powder diffraction (XRD) of the breccia reveals the presence of calcite and hematite (Fig. 7a). In the adjacent terra rossa, XRD data indicate the presence of phases consistent with kaolinite, illite, montmorillonite, and goethite (Fig. 7b). In addition to clay minerals, SEM EDS analyses detects hematite, apatite, and titanite in the terra rossa. The two major differences between the composition of the terra rossa and the inclusions of terracotta calcite are 1) the presence of Mg-rich phyllosilicates in the terra rossa and their absence in the terracotta calcite and 2) the lack of dolomite in the terra rossa and its presence in the terracotta calcite. An explanation for these differences is provided in the Paragenesis section text. Nevertheless, the terra rossa containing breccia is the likely source of inclusions in the phantom calcite.

C and O isotopes

A single sample containing a limestone clast, terracotta calcite, and colorless calcite adjacent to one another was chosen for C and O isotope analysis (Fig. S1). All three parts show distinct C and O isotope compositions (Fig. 8 and Table S1). The limestone has $\delta^{13}C$ values of ~0 ‰ and $\delta^{18}O$ values of ~-6 ‰, similar to other Triassic limestones found in the Carpathian region (Haas et al. 2006). The terracotta calcite has $\delta^{13}C$ ranging from -1 to -2 ‰, and $\delta^{18}O$ ranging from -12 to -15 ‰, whereas the colorless calcite has $\delta^{13}C$ of ~-3.5 ‰ and $\delta^{18}O$ of ~-8 ‰, indicating significant differences in the composition and/or temperature of fluid from which the terracotta calcite and colorless calcite precipitated.

Paragenesis

Based on the distinct mineralogy and isotope composition of the terracotta-colored and colorless parts of calcite we propose that these two parts precipitated from two distinct fluids. First, the terracotta-colored crystals formed from a fluid that likely carried 1) limestone-derived solutes, 2) terra rossa-derived minerals, i.e. micrometer-sized refractory particles of the terra rossa outcropping in the breccia body adjacent to the limestone (e.g., phyllosilicates, hematite) and 3) terra rossa-derived solutes.

As the calcite crystals grew, micrometer-sized terra rossa-derived mineral particles likely attached to the surfaces of growing calcite crystals, creating zones in the host calcite. In addition, a range of nanoparticles likely coprecipitated in situ on the surfaces of growing calcite crystals from terra rossa-derived solutes, including phyllosilicates, often only a few atomic layers thick. This was most probably followed by the precipitation of Fe-oxyhydroxides or dolomite on phyllosilicate nanoparticles. Here we acknowledge the ambiguity associated with discerning the

origin (transport vs. in situ precipitation) of the phases contained within both the terra cotta calcite and the parent material (e.g., hematite) based on crystal size and/or morphology alone. It is possible that the larger, micrometer-sized particles also precipitated in situ from terra rossa-derived solutes or that the smaller nanoparticles were also transported from the terra rossa.

Preferential attachment of Fe-oxyhydroxide particles to phyllosilicate nanoparticles rather than to the calcite matrix is likely due to the heterogeneously charged surfaces of clays (Tombácz and Szekeres 2006). Intimate association of magnetite nanoparticles with phyllosilicates in physical magnetic separations of marls is commonly documented in the paleomagnetic literature (e.g., Montgomery et al. 1998). A reaction mechanism by which ferric iron is sourced from larger, physically deposited clays, as opposed to electrostatic attachment onto the smaller, neoformed phyllosilicates, also is plausible as described below.

Dolomite likely grew simultaneously with the host calcite, while the fluid was still Mg-rich due to the terra rossa-derived solutes. We note that dolomite inclusions are the only Mg-bearing particles in the terracotta calcite, while Mg-rich phyllosilicates present in the terra rossa are absent from the terracotta calcite. Instead, Mg-free phyllosilicates (kaolinite and illite) are present, further supporting the idea that Mg leached from Mg-rich phyllosilicates led to the formation of dolomite. Indeed, a smectite-illite conversion has been invoked previously as the possible source of ions that form dolomites (McHargue and Price 1982) and we believe that here the same process takes place.

The smectite-illite conversion has previously been associated with neoformation of iron oxide nanocrystals (Katz et al. 1998, 2000; Woods 2002) as ferrous and ferric iron substitute in the tetrahedral and octahedral phyllosilicate sites, respectively. Although magnetite is commonly observed as the clay paragenetic iron oxide product, most studies of the magnetic effect of the

297 transition have concerned carbonaceous mudstones near reduced-fluid (volcanic) heat sources
298 (cf. also Eslinger et al. 1979), so in an oxic setting such as terra rossa limestone breccia vugs
299 hosting terracotta calcite, ferric oxyhydroxides are presumably viable phyllosilicate-conversion
300 products (Hyodo et al. 2020). It is unlikely that smectite-illite conversion is occurring in the
301 smallest, several-atomic-layers-thick phyllosilicates which are neoformed from solution as
302 described above. Larger smectites physically transported from terra rossa limestone, however,
303 plausibly liberated ferric iron to solution during conversion to illite in the hydrothermal fluid, so
304 larger hematite and goethite crystals may be neoformed by that mechanism. We note that the
305 low, negative oxygen isotope values of terracotta calcite are consistent with this elevated
306 temperature which promotes the smectite-illite conversion.
307 The formation of terracotta-colored crystals was likely followed by the precipitation of
308 colorless part of crystals from a fluid that only contained limestone-derived solutes. The lack of
309 dolomite particles in the colorless part provides further support for Mg originating from the terra
310 rossa. These lower-temperature fluids, with an intermediate oxygen isotopic composition
311 between that of marine limestone and hydrothermal terracotta calcite, were likely distributed
312 along fractures or faults associated with the formation of the breccia body. Their lower, more
313 negative carbon isotope values compared to terracotta calcite is consistent with precipitation
314 from a distilled residual fluid.
315

316 **Implications**

317

318 It has been suggested previously that phyllosilicates (e.g., smectites) promote the nucleation and
319 growth of Ca-Mg carbonate minerals (Nyirő-Kósa et al. 2018; Fodor et al. 2020). Phyllosilicate

320 nucleation on calcite and dolomite nucleation on phyllosilicates, as inferred from nanoscale
321 mineralogical associations, suggest that carbonates can also provide surfaces for the growth of
322 phyllosilicates and this mutual enhancement may result in the formation of large-scale clay-
323 carbonate successions in aqueous settings. Indeed, primary dolostones are rich in Mg-rich
324 phyllosilicates (Weber 1964; Raub et al. 2007; Bristow et al. 2011), which were proposed to play
325 a crucial role in primary dolomite formation in a diverse set of environments, including the
326 seafloor (Kahle 1965), lakes (Wanas and Sallam 2016), and soils (Díaz-Hernández et al. 2013;
327 Cuadros et al. 2016). Post-Snowball Earth cap dolostones, intriguingly, are terracotta-colored
328 and contain abundant hematite, maghemite, and oxidized magnetite carrying primary
329 magnetization and associated with ubiquitous phyllosilicates (Raub et al. 2007).
330 Our results show that dolomite precipitation is also possible in karstic environments
331 where limestone is in contact with soil (terra rossa), from fluids dissolving Ca-carbonate and
332 simultaneously leaching Mg from phyllosilicates. Recently, Mg-bearing calcium carbonate and
333 dolomite formation at ambient conditions in the presence of clays has been shown
334 experimentally (Liu et al. 2019; Molnár et al. 2021).
335 The mineralogy of inclusions in the terracotta calcite can suggest leads for the
336 development and design of composite structures, which has been long recognized as one of the
337 key approaches of making new functional materials with tailored properties (Ramamurthy and
338 Eaton 1994). Calcite, being one of the most abundant and important industrial materials and
339 biominerals, has received a great deal of attention within the materials science and engineering
340 community.
341 A wide range of organic and inorganic materials have been incorporated into the calcite
342 structure in order to control its optical, mechanical, and magnetic properties (e.g., Kim et al.,

2011; Kulak et al., 2014; Cho et al., 2016; Green et al., 2016). The latter, for instance, has been achieved by the occlusion of magnetite (Fe_3O_4) nanoparticles into a calcite single crystal matrix using a copolymer to control the homogeneous distribution of magnetite particles while limiting their aggregation and migration (Kulak et al. 2014). The distribution of inclusions in the terracotta calcite and the preferred nucleation of hematite and goethite on phyllosilicate rather than carbonate surfaces indicates that phyllosilicates have a potential to not only disrupt crystal growth and trigger the formation of cavities in the structure of the calcite host, but also to provide surface for the precipitation of different phases in the cavities and to uniformly distribute otherwise incompatible materials in the calcite host crystal. Indeed, the attachment of other oxides, including magnetite and TiO_2 nanoparticles to phyllosilicates has been observed previously (Galindo-Gonzalez et al. 2009; Zhou et al. 2012; Cai et al. 2014) and the potential application of phyllosilicates in composite structure development should therefore be further explored.

Acknowledgements

The Sedgwick Museum of Earth Sciences, University of Cambridge is acknowledged for the hematite sample. We thank Tamás G. Weiszburg for a constructive discussion as well as the anonymous reviewers and the associate editor Adam Wallace for their helpful comments and suggestions. This work was supported by the Natural Environment Research Council (grant number NE/L002507/1) and the Slovak Research and Development Agency (grant number APVV-19-0065). TEM studies were performed at the electron microscopy laboratory of the

University of Pannonia, established using grant number GINOP-2.3.3-15-2016-0009 from the European Structural and Investments Funds and the Hungarian Government.

References

Allmann, R., and Hinek, R. (2007) The introduction of structure types into the Inorganic Crystal Structure Database ICSD. Acta Crystallographica Section A: Foundations of Crystallography, 63, 412–417.

Bálintová, T., Ozdín, D., Fejdi, P., Števko, M., Gregor, M., and Stankovič, J. (2006) Mineralogické štúdium fantómových kalcitov z Gemerskej Vsi - Mineralogical study of phantom calcite from village Gemerská Ves, Slovakia (in Slovak). Mineralia Slovaca, 38, 124–130.

Beattie, I.R., and Gilson, T.R. (1970) The Single-crystal Raman Spectra of Nearly Opaque Materials. Iron(III) Oxide and Chromium(III) Oxide. Journal of the Chemical Society A: Inorganic, Physical, Theoretical, 980–986.

Bonev, I.K., Garcia-Ruiz, J.M., Atanassova, R., Otalora, F., and Petrussenko, S. (2005) Genesis of filamentary pyrite associated with calcite crystals. European Journal of Mineralogy, 17, 905–913.

Bristow, T.F., Bonifacie, M., Derkowski, A., Eiler, J.M., and Grotzinger, J.P. (2011) A hydrothermal origin for isotopically anomalous cap dolostone cements from south China. Nature, 474, 68–71.

Cai, L., Tong, M., Wang, X., and Kim, H. (2014) Influence of clay particles on the transport and retention of titanium dioxide nanoparticles in quartz sand. Environmental Science &

388 Technology, 48, 7323–7332.

389 Cho, K.R., Kim, Y.Y., Yang, P., Cai, W., Pan, H., Kulak, A.N., Lau, J.L., Kulshreshtha, P.,
390 Armes, S.P., Meldrum, F.C., and others (2016) Direct observation of mineral-organic
391 composite formation reveals occlusion mechanism. Nature Communications, 7, 1–7.

392 Cloots, R. (1991) Raman spectrum of carbonates $M^{II}CO_3$ in the 1100-1000 cm^{-1} region:
393 observation of the n_1 mode of the isotopic $(C^{16}O_2{}^{18}O)^{2-}$ ion. Spectrochimica Acta, 47A,
394 1745–1750.

395 Coelho, A.A. (2018) TOPAS and TOPAS-Academic : an optimization program integrating
396 computer algebra and crystallographic objects written in C++. Journal of Applied
397 Crystallography, 51, 210–218.

398 Couture, L. (1947) Étude des spectres de vibrations de monocristaux ioniques. In Annales de
399 physique Vol. 12, pp. 5–94. EDP Sciences.

400 Cuadros, J., Diaz-Hernandez, J.L., Sanchez-Navas, A., Garcia-Casco, A., and Yepes, J. (2016)
401 Chemical and textural controls on the formation of sepiolite, palygorskite and dolomite in
402 volcanic soils. Geoderma, 271, 99–114.

403 De La Pierre, M., Carteret, C., Maschio, L., André, E., Orlando, R., and Dovesi, R. (2014) The
404 Raman spectrum of $CaCO_3$ polymorphs calcite and aragonite: A combined experimental
405 and computational study. The Journal of Chemical Physics, 140, 164509.

406 Díaz-Hernández, J.L., Sánchez-Navas, A., and Reyes, E. (2013) Isotopic evidence for dolomite
407 formation in soils. Chemical Geology, 347, 20–33.

408 Elečko, M., Gaál, Ľ., Lexa, J., Mello, J., Pristaš, J., Vass, D., and Vozárová, A. (1985)
409 Geologická mapa Rimavskej kotliny a priľahlej časti Slovenského rudohoria 1:50 000 -
410 Geological map of the Rimava Basin and the adjacent part of the Slovak Ore Mountains

411 1:50 000 (in Slovak). GÚDŠ, Bratislava.

412 Eslinger, E., Highsmith, P., Albers, D., and De Mayo, B. (1979) Role of iron reduction in the
413 conversion of smectite to illite in bentonites in the disturbed belt, Montana. Clays and Clay
414 Minerals, 27, 327–338.

415 Farfan, G.A., and Post, J.E. (2019) Quartz from Madagascar with fuchsite phantom inclusions.
416 Journal of Gemmology, 36, 698–699.

417 Farsang, S., Facq, S., and Redfern, S.A.T. (2018) Raman modes of carbonate minerals as
418 pressure and temperature gauges up to 6 GPa and 500 °C. American Mineralogist, 103,
419 1988–1998.

420 Fodor, M.A., Ható, Z., Kristóf, T., and Pósfai, M. (2020) The role of clay surfaces in the
421 heterogeneous nucleation of calcite: Molecular dynamics simulations of cluster formation
422 and attachment. Chemical Geology, 538, 119497.

423 Gaál, Ľ. (2008) Geodynamika a vývoj jaskýň Slovenského krasu - Geodynamics and
424 development of caves in the Slovak Karst (in Slovak), 168 p. State Nature Conservancy of
425 the Slovak Republic, Slovak Caves Administration, Žilina.

426 Galindo-Gonzalez, C., Feinberg, J.M., Kasama, T., Gontard, L.C., Pósfai, M., Kósa, I., Duran,
427 J.D.G., Gil, J.E., Harrison, R.J., and Dunin-Borkowski, R.E. (2009) Magnetic and
428 microscopic characterization of magnetite nanoparticles adhered to clay surfaces. American
429 Mineralogist, 94, 1120–1129.

430 Gornitz, V. (1981) Phantom crystals. In Mineralogy. Encyclopedia of Earth Science. pp. 368–
431 369. Springer, Boston, MA.

432 Green, D.C., Ihli, J., Thornton, P.D., Holden, M.A., Marzec, B., Kim, Y.Y., Kulak, A.N.,
433 Levenstein, M.A., Tang, C., Lynch, C., and others (2016) 3D visualization of additive

434 occlusion and tunable full-spectrum fluorescence in calcite. Nature Communications, 7, 1–
435 13.
436 Haas, J., Demény, A., Hips, K., and Vennemann, T.W. (2006) Carbon isotope excursions and
437 microfacies changes in marine Permian-Triassic boundary sections in Hungary.
438 Palaeogeography, Palaeoclimatology, Palaeoecology, 237, 160–181.
439 Hyodo, M., Sano, T., Matsumoto, M., Seto, Y., Bradák, B., Suzuki, K., Fukuda, J., Shi, M., and
440 Yang, T. (2020) Nanosized authigenic magnetite and hematite particles in mature-paleosol
441 phyllosilicates: New evidence for a magnetic enhancement mechanism in loess sequences
442 of China. Journal of Geophysical Research: Solid Earth, 125, e2019JB018705.
443 Johnston, W.D., and Butler, R.D. (1946) Quartz crystal in Brazil. Bulletin of the Geological
444 Society of America, 57, 601–650.
445 Kahle, C.F. (1965) Possible Roles of Clay Minerals in the Formation of Dolomite. SEPM Journal
446 of Sedimentary Research, Vol. 35, 448–453.
447 Katz, B., Elmore, R.D., and Engel, M.H. (1998) Authigenesis of magnetite in organic-rich
448 sediment next to a dike: Implications for thermoviscous and chemical remagnetizations.
449 Earth and Planetary Science Letters, 163, 221–234.
450 Katz, B., Elmore, R.D., Cogoini, M., Engel, M.H., and Ferry, S. (2000) Associations between
451 burial diagenesis of smectite, chemical remagnetization, and magnetite authigenesis in the
452 Vocontian trough, SE France. Journal of Geophysical Research: Solid Earth, 105, 851–868.
453 Kim, Y.Y., Ganesan, K., Yang, P., Kulak, A.N., Borukhin, S., Pechook, S., Ribeiro, L., Kröger,
454 R., Eichhorn, S.J., Armes, S.P., and others (2011) An artificial biomineral formed by
455 incorporation of copolymer micelles in calcite crystals. Nature Materials, 10, 890–896.
456 Krishnamurti, D. (1957) The Raman spectrum of calcite and its interpretation. Proceedings of the

Indian Academy of Sciences - Section A, 44, 183–202.

Krishnan, R.S. (1945) Raman spectra of the second order in crystals Part I: Calcite. Proceedings of the Indian Academy of Sciences - Section A, 182–192.

Kulak, A.N., Semsarilar, M., Kim, Y.-Y., Ihli, J., Fielding, L.A., Cespedes, O., Armes, S.P., and Meldrum, F.C. (2014) One-pot synthesis of an inorganic heterostructure: uniform occlusion of magnetite nanoparticles within calcite single crystals. Chem. Sci., 5, 738–743.

Liu, D., Xu, Y., Papineau, D., Yu, N., Fan, Q., Qiu, X., and Wang, H. (2019) Experimental evidence for abiotic formation of low-temperature proto-dolomite facilitated by clay minerals. Geochimica et Cosmochimica Acta, 247, 83–95.

Massey, M.J., Baier, U., Merlin, R., and Weber, W.H. (1990) Effects of pressure and isotopic substitution on the Raman spectrum of α-Fe_2O_3: Identification of two-magnon scattering. Physical Review B, 41, 7822–7827.

McCarty, K.F., and Boehme, D.R. (1989) A Raman Study of the Systems $Fe_{3-x}Cr_xO_4$ and $Fe_{2-x}Cr_xO_3$. Journal of Solid State Chemistry, 79, 19–27.

McCrea, J.M. (1950) On the isotopic chemistry of carbonates and a paleotemperature scale. The Journal of Chemical Physics, 18, 849–857.

McHargue, T.R., and Price, R.C. (1982) Dolomite from clay in argillaceous or shale-associated marine carbonates. Journal of Sedimentary Petrology, 52, 873–886.

Molnár, Z., Pekker, P., Dódony, I., and Pósfai, M. (2021) Clay minerals affect calcium (magnesium) carbonate precipitation and aging. Earth and Planetary Science Letters, 567, 116971.

Montgomery, P., Hailwood, E.A., Gale, A.S., and Burnett, J.A. (1998) The magnetostratigraphy of Coniacian-Late Campanian chalk sequences in southern England. Earth and Planetary

480 Science Letters, 156, 209–224.

481 Németh, T., Máthé, Z., Pekker, P., Dódony, I., Kovács-Kis, V., Sipos, P., Cora, I., and Kovács, I.

482 (2016) Clay mineralogy of the Boda Claystone Formation (Mecsek Mts., SW Hungary).

483 Open Geosciences, 8, 259–274.

484 Nyirő-Kósa, I., Rostási, Á., Bereczk-Tompa, É., Cora, I., Koblar, M., Kovács, A., and Pósfai, M.

485 (2018) Nucleation and growth of Mg-bearing calcite in a shallow, calcareous lake. Earth

486 and Planetary Science Letters, 496, 20–28.

487 Ramamurthy, V., and Eaton, D.F. (1994) Perspectives on Solid-State Host-Guest Assemblies.

488 Chemistry of Materials, 6, 1128–1136.

489 Raub, T.D., Evans, D.A.D., and Smirnov, A. V. (2007) Siliciclastic prelude to Elatina-

490 Nuccaleena deglaciation: Lithostratigraphy and rock magnetism of the base of the

491 Ediacaran system. Geological Society Special Publication, 286, 53–76.

492 Rehtijärvi, P., and Kinnunen, K.A. (1979) Fluid and mineral inclusions and inclusion zones of

493 cave calcite from Korsnäs mine, western Finland. Bull. Geol. Soc. Finland, 51, 75–79.

494 Saloman, E.B., and Sansonetti, C.J. (2004) Wavelengths, energy level classifications, and energy

495 levels for the spectrum of neutral neon. Journal of Physical and Chemical Reference Data,

496 33, 1113–1158.

497 Shim, S.-H., and Duffy, T.S. (2001) Raman spectroscopy of Fe_2O_3 to 62 GPa. American

498 Mineralogist, 87, 318–326.

499 Sinkankas, J. (1966) Mineralogy: a first course. D. Van Nostrand Company, Princeton, New

500 Jersey.

501 Tombácz, E., and Szekeres, M. (2006) Surface charge heterogeneity of kaolinite in aqueous

502 suspension in comparison with montmorillonite. Applied Clay Science, 34, 105–124.

503 Wanas, H.A., and Sallam, E. (2016) Abiotically-formed, primary dolomite in the mid-Eocene
504 lacustrine succession at Gebel El-Goza El-Hamra, NE Egypt: An approach to the role of
505 smectitic clays. Sedimentary Geology, 343, 132–140.
506 Weber, J.N. (1964) Carbon isotope ratios in dolostones: some implications concerning the
507 genesis of secondary and "primary" dolostones. Geochimica et Cosmochimica Acta, 28,
508 1257–1265.
509 Woods, S.D. (2002) Paleomagnetic dating of the smectite-to-illite conversion: Testing the
510 hypothesis in Jurassic sedimentary rocks, Skye, Scotland. Journal of Geophysical Research,
511 107.
512 Zhou, D., Abdel-fattah, A.I., and Keller, A.A. (2012) Clay Particles Destabilize Engineered
513 Nanoparticles in Aqueous Environments. Environmental Science & Technology, 26, 7520–
514 7526.
515

516 **List of figures**

517

518 Figure 1. Phantom calcite from Gemerská Ves, Slovakia.

519

520 Figure 2. Rocks of the outcrop: a) limestone – breccia contact. The breccia contains limestone
521 clasts and terra rossa rich layers, b) sample of breccia coming from the edge of the body, c) the
522 center of the body with vugs and d) sample of breccia coming from the center of the body. The
523 coin for scale has a diameter of 23.25 mm.

524

525 Figure 3. Raman spectra of a-b) colorless part of calcite, c-d) terracotta part of calcite, and e)
526 hematite. b) and d) show the absence and presence of low-intensity features in a) and c),
527 respectively.

528

529 Figure 4. a) cavity- and particle-rich zones in terracotta calcite, b) boundary between the
530 colorless, cavity- and particle-free calcite and the terracotta-colored, cavity- and particle-rich
531 calcite, c-f) particles in the terracotta-colored calcite: c) and d) dolomite, e) phyllosilicate, and f)
532 apatite. Ap = apatite, Cal = calcite, Dol = dolomite, Hem = hematite, Phy = phyllosilicate. BSE
533 images.

534

535 Figure 5. a) STEM HAADF image and b) combined EDS element map of a hematite-rich region.
536 High concentrations of Mg correspond to dolomite, Si to phyllosilicate, P to apatite, and Fe to
537 hematite. c) HRTEM image showing the intimate relationship between calcite, phyllosilicates,
538 and hematite. Ap = apatite, Cal = calcite, Dol = dolomite, Hem = hematite, Phy = phyllosilicate.

539

540 Figure 6. a) STEM HAADF image and b) HR STEM HAADF image of hematite and its Fourier
541 Transform (FT) image with Miller indices indicated. The hematite grows on a phyllosilicate
542 attached to the walls of a cavity in calcite. c) HRTEM image of goethite with phyllosilicate and
543 calcite and the FT image of the goethite with Miller indices indicated. d) HR STEM HAADF
544 image of goethite with phyllosilicate and the FT image of the goethite with Miller indices
545 indicated. Cal = calcite, Gth = goethite, Hem = hematite, Phy = phyllosilicate.

546

547 Figure 7. XRD pattern of phases in a) breccia: calcite, hematite, and quartz; and b) terra rossa:
548 kaolinite, illite, montmorillonite, goethite, and quartz. Quartz is most likely contamination.

549

550 Figure 8. C and O isotope data. The numbers next to data points corresponding to points of
551 analysis in Figure S1.


5 mm

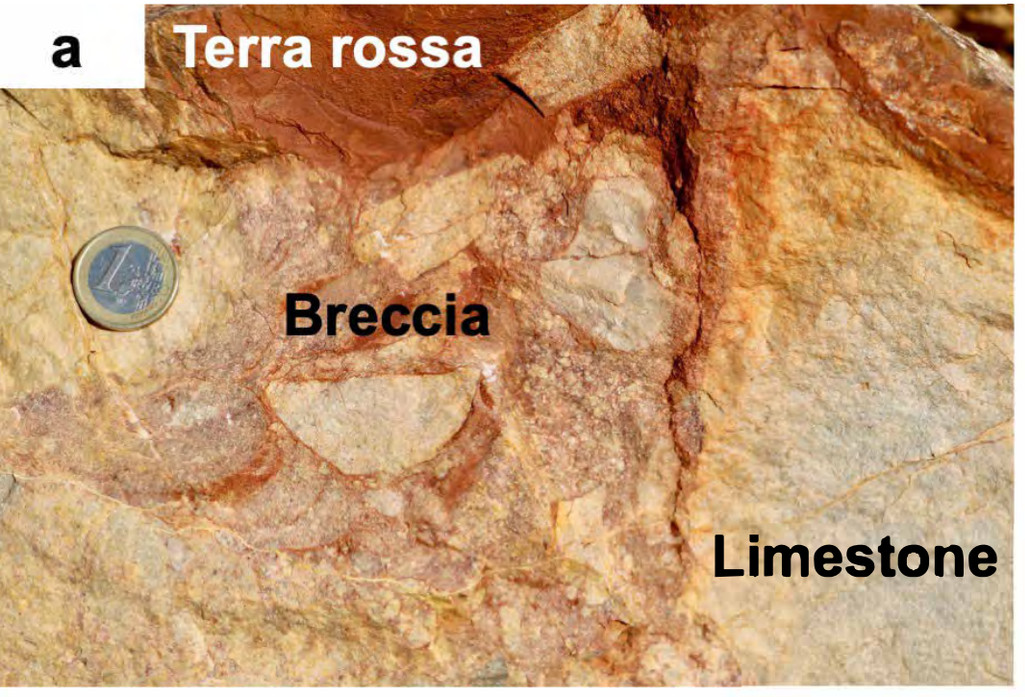
a
Terra rossa
Breccia
Limestone


b
Terra rossa
Breccia


c


d

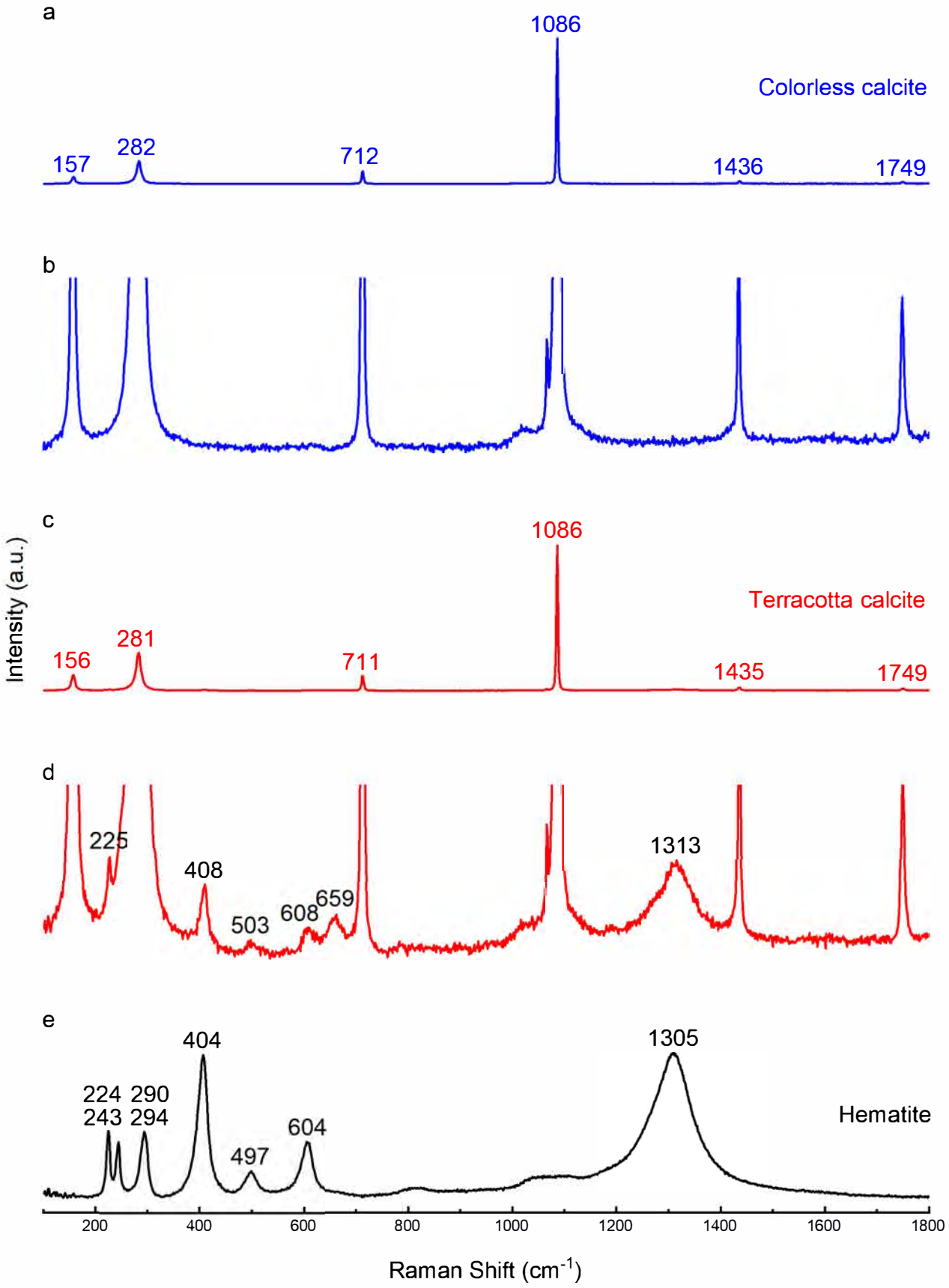
a
1086
Colorless calcite
157
282
712
1436
1749
b
c
1086
Terracotta calcite
156
281
711
1435
1749
Intensity (a.u.)
d
225
408
503
608
659
1313
e
404
1305
224 290
243 294
604
497
Hematite
200
400
600
800
1000
1200
1400
1600
1800
Raman Shift (cm-1)

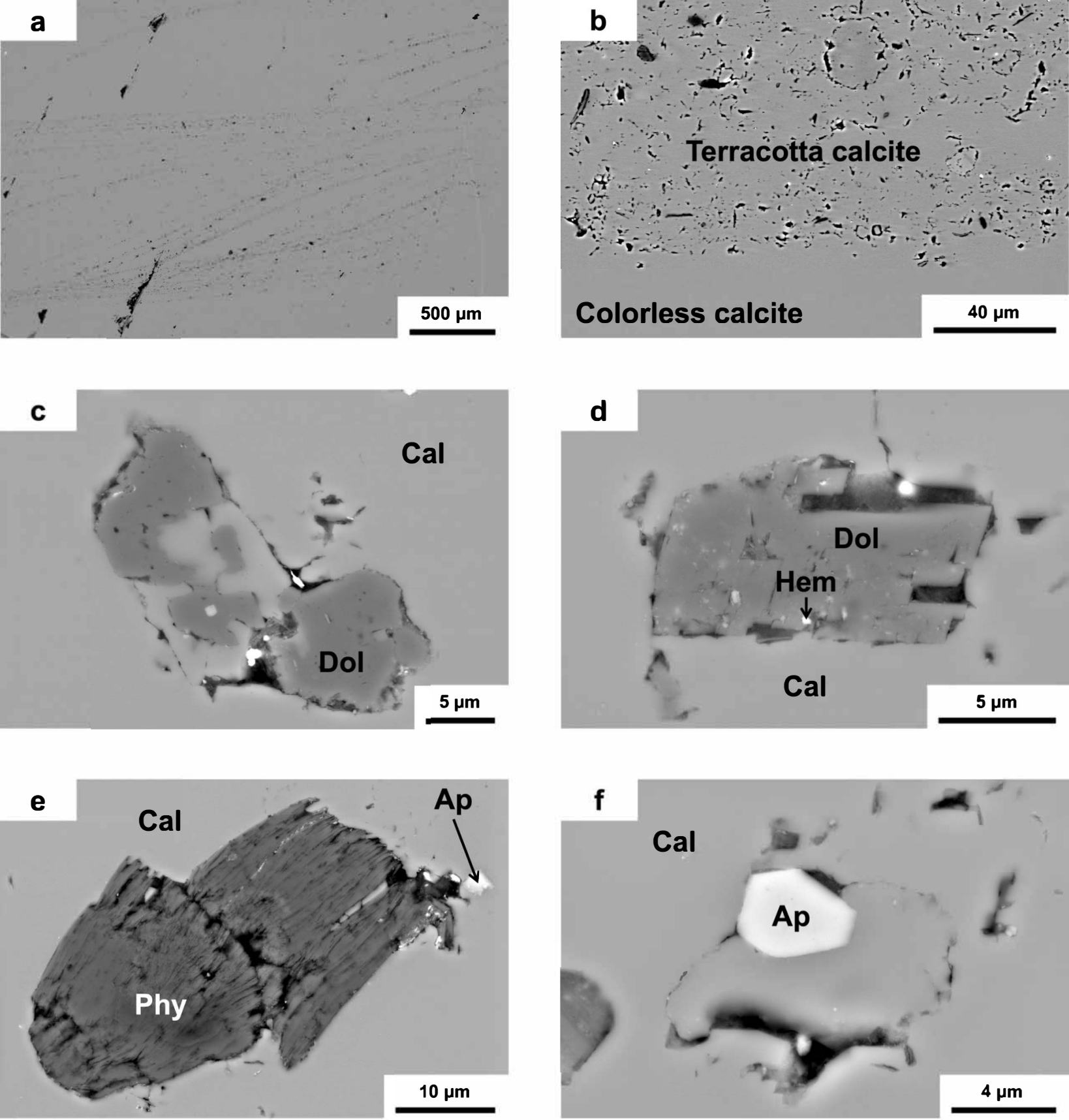
a
500 µm
b
Terracotta calcite
Colorless calcite
40 µm
c
Cal
Dol
5 µm
d
Dol
Hem
Cal
5 µm
e
Cal
Ap
Phy
10 µm
f
Cal
Ap
4 µm

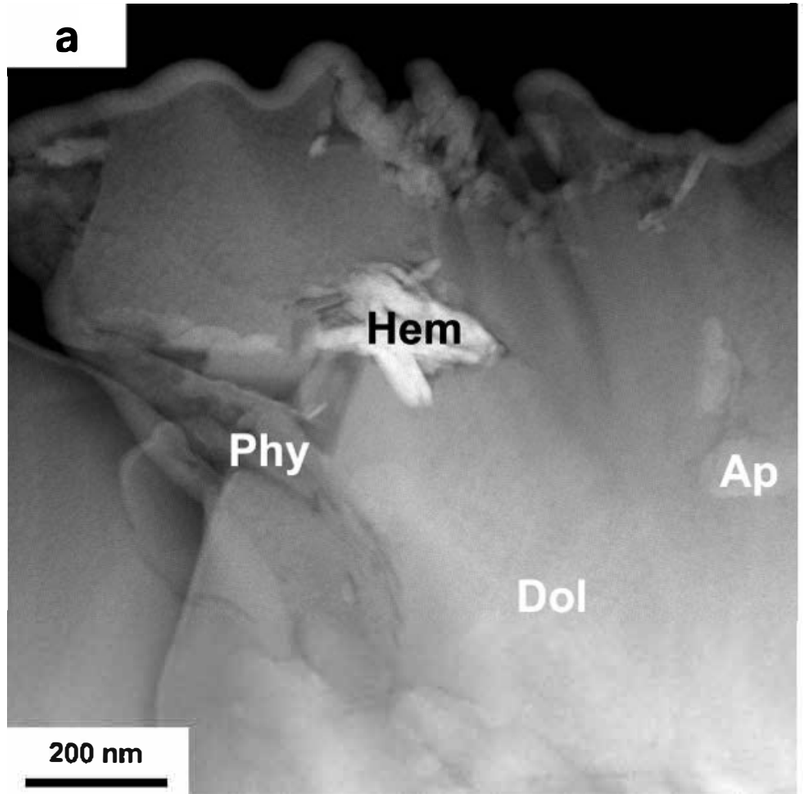
a
Hem
Phy
Ap
Dol
200 nm

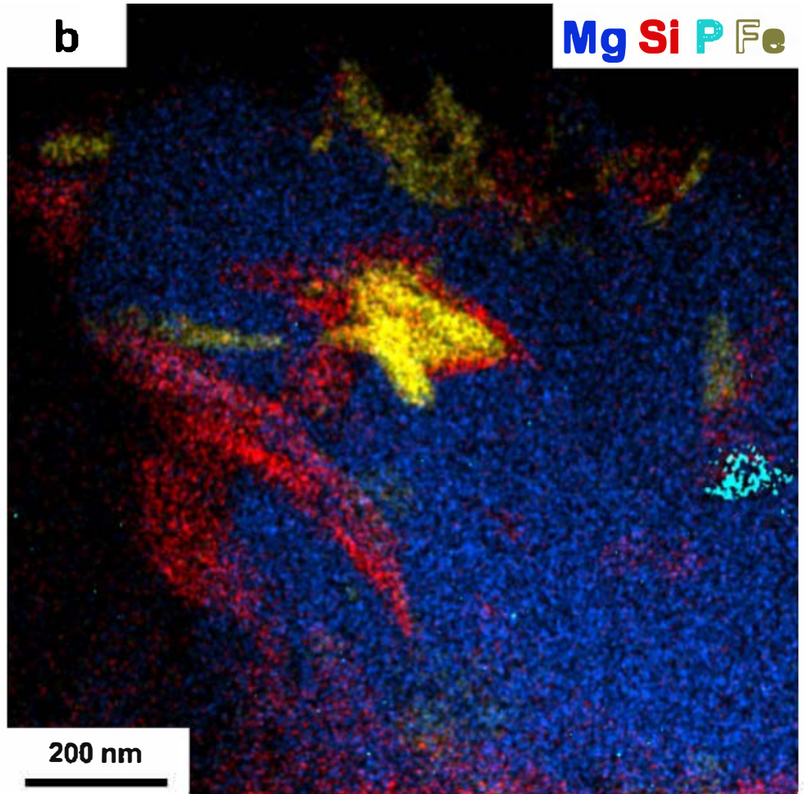
b
Mg Si P Fe
200 nm

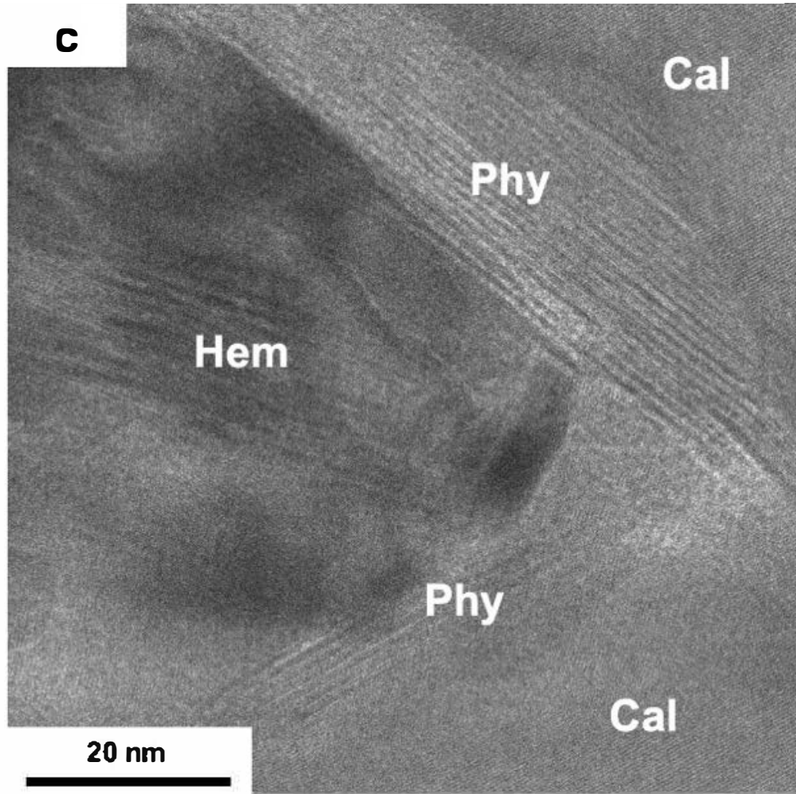
c
Cal
Phy
Hem
Phy
Cal
20 nm

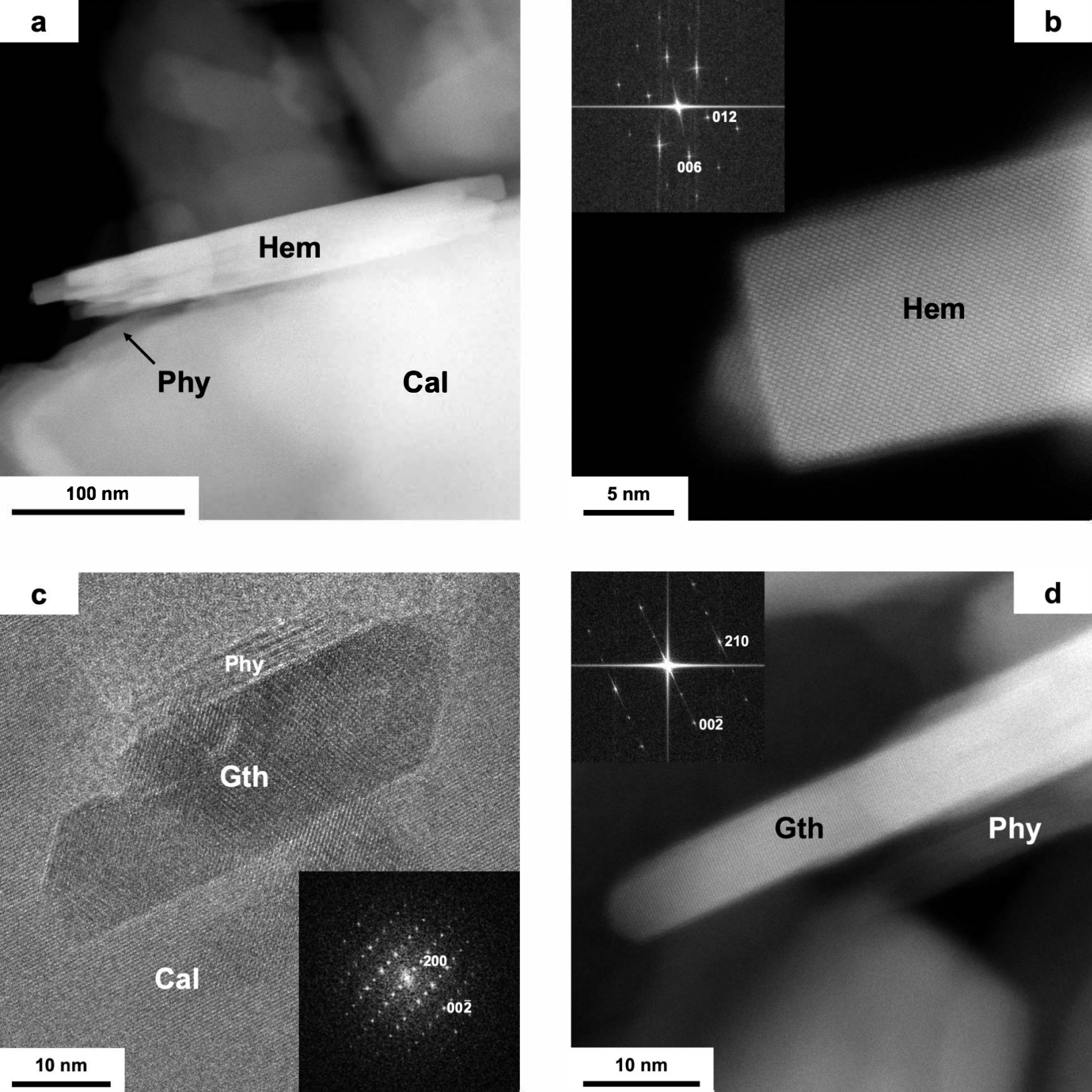
a
Hem
Phy
Cal
100 nm
b
012
006
Hem
5 nm
c
Phy
Gth
Cal
200
002̄
10 nm
d
210
002̄
Gth
Phy
10 nm

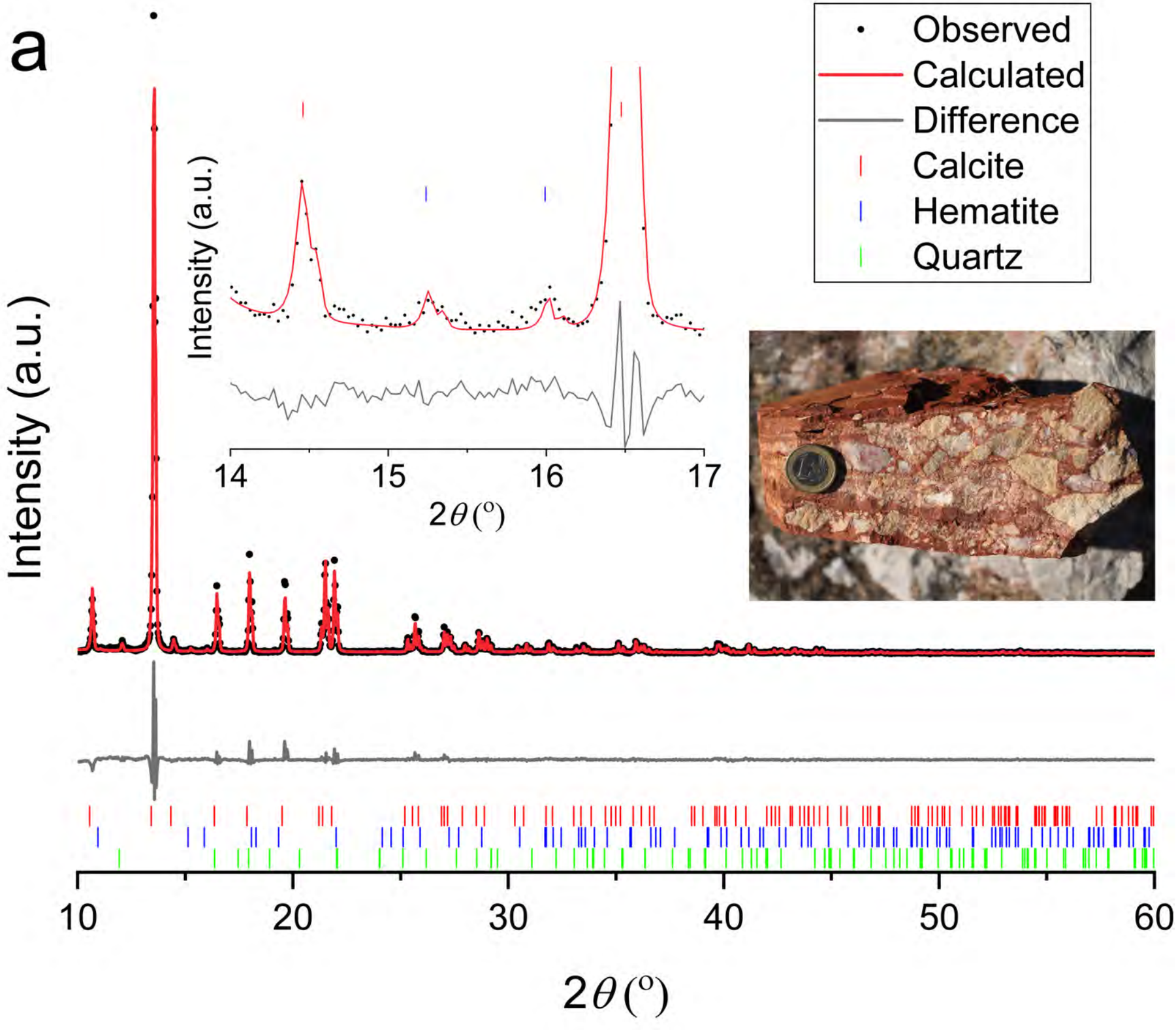
a
Observed
Calculated
Difference
Calcite
Hematite
Quartz
Intensity (a.u.)
Intensity (a.u.)
14
15
16
17
2θ(°)
10
20
30
40
50
60
2θ(°)

b

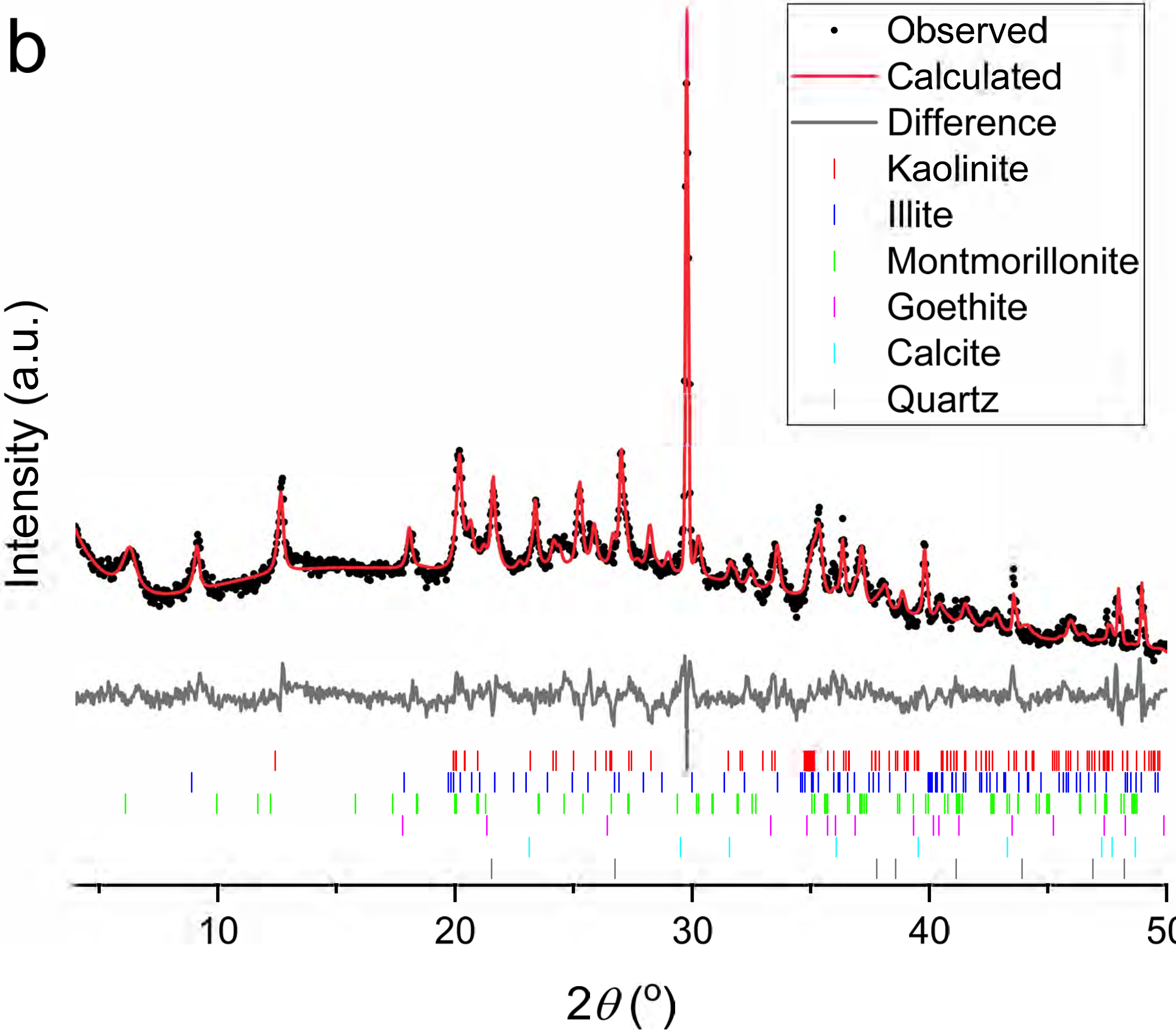
Observed
Calculated
Difference
Kaolinite
Illite
Montmorillonite
Goethite
Calcite
Quartz
Intensity (a.u.)
10
20
30
40
50
2θ (°)

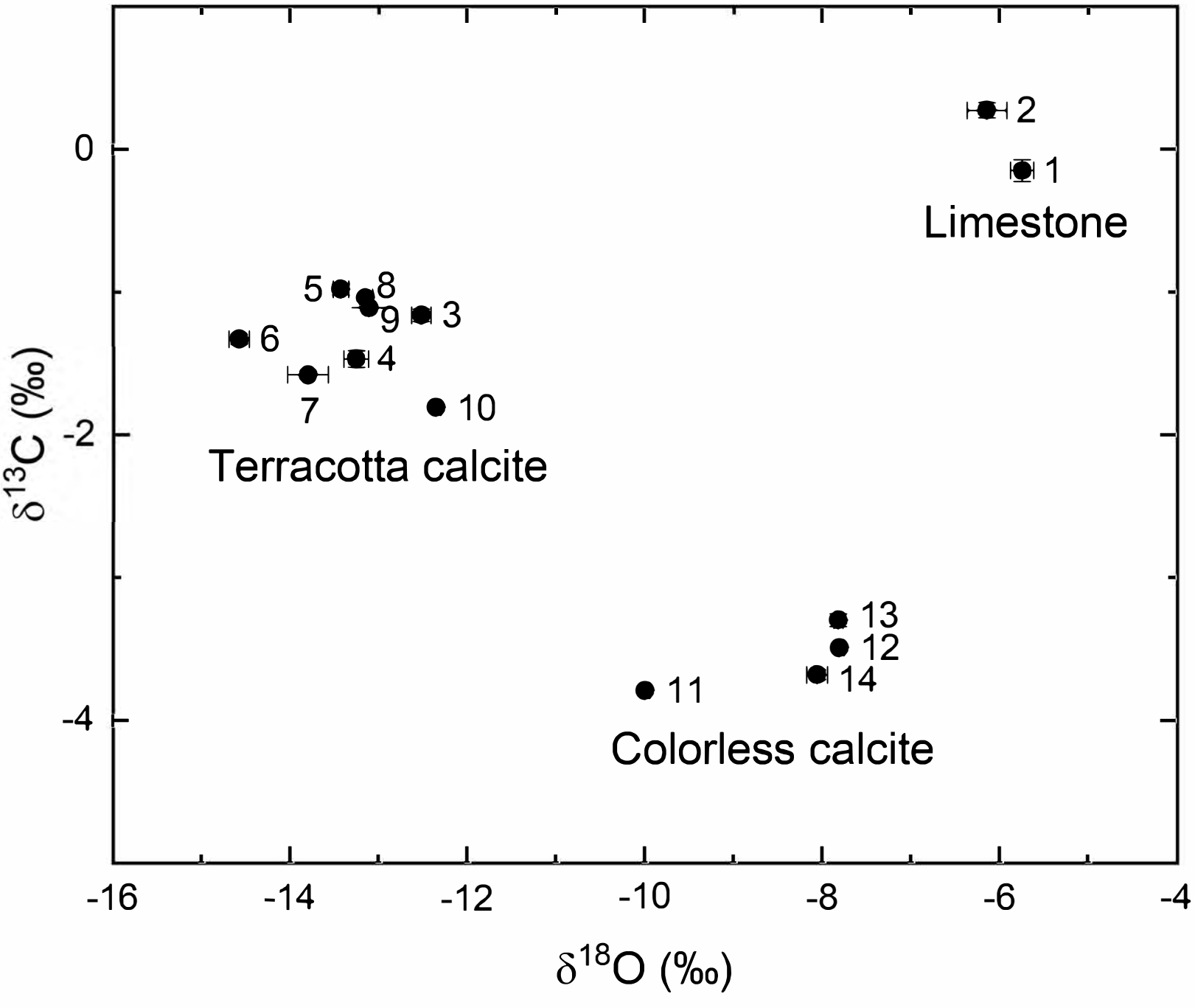
0
-2
-4
-16
-14
-12
-10
-8
-6
-4
δ13C (‰)
δ18O (‰)
2
1
Limestone
5
8
9
3
6
4
7
10
Terracotta calcite
13
12
14
11
Colorless calcite